

Numerical Algorithm for the Biermann Effect in ICF Self-generated Magnetic Fields and Its Applications

Yang Rong, Song Peng, and Wang Qiang(✉)

Institute of Applied Physics and Computational Mathematics, Beijing, China
{yang_rong,song_peng,wang_qiang}@iapcm.ac.cn

Abstract. A numerical algorithm is conducted based on a two-dimensional cylindrical coordinate system for the Biermann-Battery effect in the self-generated magnetic field of ICF. The numerical calculation of the Biermann-Battery term is highly prone to generating large non-physical strong magnetic fields due to pressure jumps and density discontinuities. A finite volume discrete scheme based on arbitrary quadrilateral meshes is designed, and a nodal quantity interpolation method suitable for practical application problems is presented. Furthermore, a new discrete scheme for suppressing oscillations is developed. The accuracy and oscillation suppression effect of the scheme are tested on general distorted meshes. Simulations of typical model problems are carried out, and qualitatively reasonable magnetic field distributions are obtained.

Keywords: self-generated magnetic field · Biermann Effect · arbitrary quadrilateral grid

1 Introduction

The self-generated magnetic field in laser-driven inertial confinement fusion (ICF) will greatly affect the electron heat conduction, and then affect the plasma parameter distribution and implosion symmetry in the black hohraum. Meanwhile, the applied magnetic field can optimize the laser-plasma interaction and implosion physics, which may reduce the ignition energy threshold and increase the fusion gain.

The Lasnex and Hydra programs have already included complete magnetic field program packages since the 1980 s and 1990 s. When considering the magnetic field modeling in the simulation of some typical problems, the numerical results were closer to the experimental results [1–5]. Therefore, it is necessary and very important to develop numerical simulations including magnetic field effects in radiation hydrodynamics programs.

This report mainly introduces the mathematical modeling of ICF laser fusion considering the magnetic field effect, focusing on the Biermann effect, and carries out the relevant numerical algorithm research based on the two-dimensional

© The Author(s), under exclusive license to Springer Nature Switzerland AG 2027
O. Gervasi et al. (Eds.): ICCSA 2026, LNCS 16767, pp. 96–109, 2027.
https://doi.org/10.1007/978-3-032-30491-9_7

cylindrical geometry program, as well as the numerical discrete schemes and related technologies adopted. It mainly includes the design of two finite volume schemes based on the arbitrary quadrilateral grids, the interpolation of nodal quantities, and their application effects in suppressing magnetic field oscillations in numerical simulations. Additionally, the accuracy of the algorithms is examined by the typical test cases, and the numerical simulation results of the algorithms in typical application models are provided.

The structure of this paper is arranged as follows: The second section of this paper gives a basic description of the governing equations. The third section elaborates on the physical mechanism of the Biermann effect. The fourth section details the design of two discrete schemes. The fifth section demonstrates the robustness of the schemes through numerical examples, Finally, the conclusions are presented in the last part.

2 Numerical Algorithm of the Coupled System

Considering the case of self-generated magnetic field, the evolution equation for the magnetic field is:

$$\begin{aligned}\frac{\partial \mathbf{B}}{\partial t} = \nabla \times (\mathbf{u} \times \mathbf{B}) - \nabla \times \left(\frac{c}{4\pi n_e e}(\nabla \times \mathbf{B}) \times \mathbf{B}\right) + \nabla \times \left(\frac{1}{n_e e}\nabla P_e\right) \\ -\frac{c^2}{4\pi}\nabla \times [\vec{\eta} \cdot (\nabla \times \mathbf{B})] + \frac{1}{4\pi e}\nabla \times [\overleftrightarrow{\beta} \cdot (\nabla \times \mathbf{B})].\end{aligned} \tag{1}$$

The first term on the right side of the equation is the magnetic field Lorentz force, also known as the magnetic freezing term; the second term is the Hall term, which represents the magnetic field generated by the macroscopic motion of the electron, the third term is the electron heat pressing term, also known as the Biermann-Battery term, the fourth term is the resistance diffusion term, and the fifth term is the Nernst term. The effect of self-generated magnetic field has a great influence on the electron and ion equations in radiation hydrodynamics equations. The electron and ion equations are as follows:

$$\begin{aligned}\frac{\partial \varepsilon_e}{\partial t} + \nabla \cdot (\varepsilon_e u) = -P_e \nabla \cdot \mathbf{u} - \nabla \cdot \left(-\vec{\kappa}_e \cdot \nabla(k_B T_e) - \frac{(k_B T_e)}{e}\overleftrightarrow{\beta} \cdot \mathbf{J}\right) - W_{er} - W_{ei} \\ +(\vec{\eta} \cdot \mathrm{J} - \frac{1}{e}\overleftrightarrow{\beta} \cdot \nabla T_e) \cdot \mathrm{J} - P_e \nabla \cdot \left(\frac{\mathrm{J}}{e n_e}\right) - \nabla \cdot \left(\frac{\varepsilon_e \mathrm{J}}{e n_e}\right).\end{aligned} \tag{2}$$

$$\frac{\partial \varepsilon_i}{\partial t} = -P_i \nabla \cdot \mathbf{u}_i - \nabla \cdot \left(-\vec{\kappa}_i \cdot \nabla(k_B T_i)\right) - W_{ie} + W_{iF}. \tag{3}$$

In Eqs. (1)–(3), the magnetic field transport coefficients, electron and ion heat flux coefficients are all anisotropic tensor forms, and their specific functional expressions are given by Braginskii's [6] model.

While self-generated magnetic field coupling radiation fluid dynamics equations, the whole system equation is complex. Aimed at this system, a set of applicable numerical solution algorithm is given. First, a split scheme is adopted to reduce the complexity; the whole system is divided into two parts: the fluid

and energy equations. The self-generated magnetic field mainly affects the energy equation. For the energy system, based on the speed change of the physical mechanism, the magnetic field equation and its influence on the electron equation are solved first, and then the radiation, electron and ion coupling systems are solved.

In this study, the Biermann-Battery term of magnetic field is studied. It is the cross product of the pressure and electron number density to generate the magnetic field source, and the electron number density and pressure have strong discontinuities at the material interface and near the shock wave, which will easily produce a numerical strong magnetic field and oscillation, particularly for arbitrary quadrilateral grids [7–11].

3 Biermann-Battery Effect

The Biermann-Battery effect arises from the significant mass difference between electrons and ions, attributable to microscopic charge separation in plasmas: pressure accelerates electrons far more strongly than ions, and the relative acceleration between the two components induces charge separation, which requires the electric field to satisfy an equilibrium condition.

$$-\nabla P_e - en_e \mathrm{E} = 0,$$

where n_e and P_e are the electron number density and pressure, respectively. Substituting the ideal gas equation of state into the momentum equation yields the expression for the electric field strength. Further substituting this into Maxwell's equations gives

$$\frac{\partial B}{\partial t} = \frac{ck_B}{en_e} \nabla T_e \times \nabla n_e.$$

In the induction equation, it serves as a magnetic field source term, generating a non-zero magnetic field from an initially unmagnetized state when the directions of temperature gradient and density gradient in the plasma are misaligned. For instance, in ICF laser ablation, plasma expansion occurs primarily along the target surface normal direction. Consequently, the electron density gradient mainly aligns perpendicular to the target surface. However, since electron thermal conduction at the target surface contributes more significantly to temperature than plasma adiabatic expansion, the electron temperature gradient predominantly lies parallel to the target surface. As shown in Fig. 1, irradiation non-uniformity at the focal spot will exacerbate this misalignment. The thermoelectric field generated by this misalignment between temperature and density gradients will drive currents, inducing a quasi-static self-generated magnetic field. This quasi-static magnetic field exhibits a toroidal structure, as illustrated in Fig. 2. To estimate the strength of such magnetic fields, it is assumed that $\frac{\partial B}{\partial t} \sim \frac{1}{\tau_L}$, $\frac{\nabla n_e}{n_e} \sim \frac{1}{L_n}$, $\frac{\nabla T_e}{T_e} \sim \frac{1}{L_T}$, then $B[\mathrm{MGauss}] = 10(\frac{\tau_L}{1\mathrm{ns}})(\frac{T_e}{1\mathrm{keV}})(\frac{30\mu m}{L_n})$. Self-generated toroidal magnetic fields at the mega-gauss (hundred-tesla) level can be produced in hohlraum plasmas.

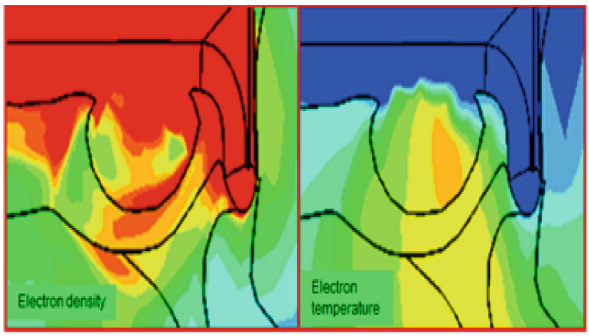


Fig. 1. Electron density and temperature distributions near the laser irradiation spot within the implosion cavity.

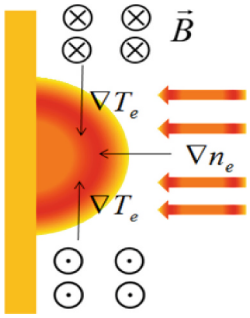


Fig. 2. Schematic diagram of toroidal magnetic field generation by thermoelectric mechanism.

In the cylindrical coordinate system, when focusing on a toroidal magnetic field, represented as $\mathbf{B} = (0, B_\theta, 0)$, and assuming $\frac{\partial B_\theta}{\partial \theta} \sim 0$. The equation $\nabla \cdot \mathbf{B} = 0$ is inherently fulfilled. At this point, the scalar form of the magnetic field equation in two-dimensional cylindrical geometry can be written as

$$\begin{aligned} &\frac{dB_\theta}{dt} = -\frac{c\partial}{e\partial r}\left(\frac{1}{n_e}\frac{\partial P_e}{\partial z}\right) + \frac{c\partial}{e\partial z}\left(\frac{1}{n_e}\frac{\partial P_e}{\partial r}\right) + \\ &\frac{c^2}{4\pi}\left(\frac{\partial}{\partial r}\left(\frac{\eta_\perp}{r}\frac{\partial (rB_\theta)}{\partial r} - \frac{\eta^\wedge}{r}\frac{\partial (rB_\theta)}{\partial z}\right) + \frac{\partial}{\partial z}\left(\frac{\eta_\perp}{r}\frac{\partial (rB_\theta)}{\partial z} + \frac{\eta^\wedge}{r}\frac{\partial (rB_\theta)}{\partial r}\right)\right). \end{aligned} \tag{4}$$

4 Numerical Algorithm of Biermann-Battery Term

To adapt for coupling with the radiation hydrodynamics equations, Eq. (4) are discretized using a finite volume scheme on arbitrary quadrilateral grids generated by two-dimensional fluid motions.

Assume the computational domain is a bounded two-dimensional regionΩ, partitioned into several mutually non-overlapping arbitrary structured quadrilateral grids. The full-integer indices (i, j) denote grid node coordinates, while the half-integer indices $(i + 1/2, j + 1/2)$ represent cell centroids. An arbitrary quadrilateral cell formed by nodes $(i, j), (i + 1, j), (i + 1, j + 1)$, and $(i, j + 1)$ is designated as grid cell K. The four edges of cell K are denoted as $K_l, l = 1, \cdots, 4$ (as shown in Fig. 3).

The magnetic field equation is discretized by a finite volume scheme. First, integrate Eq. (4) over the solid of revolution formed by the partitioned arbitrary quadrilateral cell in region. The first term on the right-hand side represents the magnetic resistive diffusion term, which is discretized by the classical nine-point diffusion scheme. This paper primarily focuses on the second term, the Biermann-Battery term, so that we neglect the magnetic resistive diffusion term. Thus, we

have

$$\int_{K_{i,j}} \frac{\partial \mathbf{B}}{\partial t} dV = \int_{K_{i,j}} \nabla \times (\frac{1}{n_e e} \nabla P_e) dV \tag{5}$$

The Eq. (5) is integrated over each cell K and the Gauss divergence formula is used to obtain:

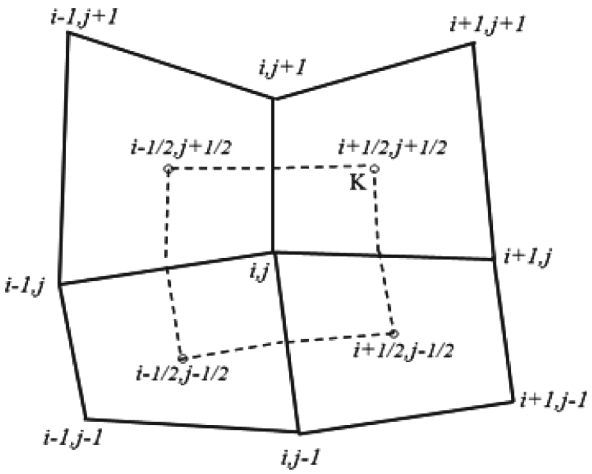


Fig. 3. Mesh Partition.

$$\begin{aligned}
&\frac{c}{e} \int_K r(-\frac{\partial}{\partial r}\left(\frac{1}{n_e}\frac{\partial P_e}{\partial z}\right) + \frac{\partial}{\partial z}\left(\frac{1}{n_e}\frac{\partial P_e}{\partial r}\right))dzdr \\
&= r_{i+1/2,j+1/2}\frac{c}{e}\oint_K \left(\frac{1}{n_e}\frac{\partial P_e}{\partial z}\right)dz + \left(\frac{1}{n_e}\frac{\partial P_e}{\partial r}\right)dr \\
&= r_{i+1/2,j+1/2}\frac{c}{e}\sum_{l=1}^{4}\left(\frac{1}{n_{e\,K^{l+1/2}}}\right)(P_{eK^{l,i+1,j}} - P_{eK^{l,ij}})
\end{aligned} \tag{6}$$

In the above formula, $r_{i+1/2,j+1/2}$represents the r-coordinate at the grid cell center. $K^{l+1/2}$denotes the edge-centered quantity of the $l-th$ edge in grid cell K. Therefore, $K^{l,ij}$and $K^{l,i+1,j}$respectively represent the starting and ending points of the $k-th$ edge along the counterclockwise direction of grid cell. This scheme requires node-centered pressure quantities and edge-centered electron number densities. Since the magnitude of the electron number density is extremely large, directly applying this formula would introduce significant numerical errors. In practical computations, we apply an identity transformation to the thermal pressure term:

$$\nabla \times (\frac{c}{n_e e}\nabla P_e) = \frac{c}{e}\nabla \times (\frac{1}{n_e}P_e \nabla \ln n_e) \tag{7}$$

Similarly, using loop integration, we have

$$\begin{aligned}
&\frac{c}{e}\int_K r(-\frac{\partial}{\partial r}\left(\frac{1}{n_e}\frac{\partial P_e}{\partial z}\right)+\frac{\partial}{\partial z}\left(\frac{1}{n_e}\frac{\partial P_e}{\partial r}\right))dzdr \\
&= r_{i+1/2,j+1/2}\frac{c}{e}\oint_K\left(\frac{1}{n_e}\frac{\partial P_e}{\partial z}\right)dz+\left(\frac{1}{n_e}\frac{\partial P_e}{\partial r}\right)dr \\
&= r_{i+1/2,j+1/2}\frac{c}{e}\sum_{l=1}^{4}\left(\frac{P_e}{n_e}\right)_{K^{l+1/2}}\left(\ln n_{eK^{l,i+1,j}}-\ln n_{eK^{l,ij}}\right)
\end{aligned} \tag{8}$$

In practical simulation applications, the electron number density and pressure may exhibit strong discontinuities near interfaces due to factors such as multi-material interactions, shock waves, and equation-of-state jump discontinuities. Direct application of this formula would lead to nonphysical numerical solutions. Figure 4 simulates a laser ablation Au planar target model, which theoretically should generate negative magnetic fields as illustrated in Fig. 2. However, numerical simulations using Formula (8) produce nonphysical positive magnetic fields due to equation-of-state discontinuities.

Considering the material pressure using the ideal gas equation of state, we have:$P_e = k_B n_e T_e$, then$\frac{P_e}{n_e} = k_B T_e$. Material temperature remains continuous across discontinuities, and the Biermann-Battery term can be expressed as

$$\nabla\times(\frac{c}{n_e e}\nabla P_e)=\frac{c}{e}\nabla\times(k_B T_e\nabla\ln n_e) \tag{9}$$

The final discrete form using loop integration can be written as Eq. (10), referred to as original scheme or scheme1, it can avoid the above nonphysical numerical case.

$$\begin{aligned}
&\frac{c}{e}\int_K r(-\frac{\partial}{\partial r}\left(\frac{1}{n_e}\frac{\partial P_e}{\partial z}\right)+\frac{\partial}{\partial z}\left(\frac{1}{n_e}\frac{\partial P_e}{\partial r}\right))dzdr \\
&= r_{i+1/2,j+1/2}\frac{c}{e}\oint_K\left(\frac{1}{n_e}\frac{\partial P_e}{\partial z}\right)dz+\left(\frac{1}{n_e}\frac{\partial P_e}{\partial r}\right)dr \\
&= r_{i+1/2,j+1/2}\frac{c}{e}\sum_{l=1}^{4}\left(k_B T_e\right)_{K^{l+1/2}}\left(\ln n_{eK^{l,i+1,j}}-\ln n_{eK^{l,ij}}\right)
\end{aligned} \tag{10}$$

4.1 Interpolation of Node Quantity

In the calculation of scheme (10), the discretization involves edge-centered temperature quantities, node-centered electron number densities. For any node Q_i surrounded by four cell centers $K_i(i=1,2,3,4)$, their corresponding unknown quantities are denoted as $u_0, u_i(i=1,2,3,4)$. The general interpolation of electron number density employs mass-weighted averaging of surrounding cells

$$u_0=\sum_{i=1}^{4}w_i u_i,$$

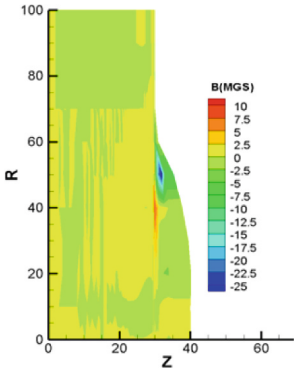


Fig. 4. Non-physical magnetic field obtained by Formula (8).

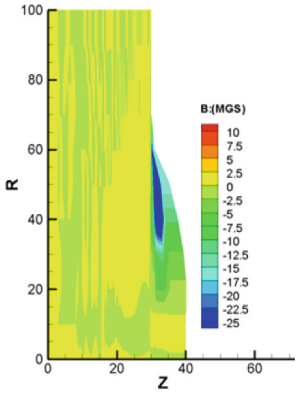


Fig. 5. Reasonable magnetic field distribution by Formula (10).

where $w_i = \dfrac{m_i}{\sum_{i=4} m_i}$. When simulating multi-material problems involving light-heavy materials, the mass-weighted averaging may introduce significant defects near interfaces: the effective density weighting of light-material cells is reduced. Near light-heavy material interfaces, this implies $n_e^{node} \approx n_e^{heavy}$. Consequently, in light-material cells$n_e^{node} \approx n_e^{heavy} \gg n_e^{light}$, and nonphysically steep gradients emerge in the low-density regions. Prolonged accumulation of these errors causes continuous growth of magnetic field strength near interfaces (Fig. 6). This ultimately leads to numerical divergence (Fig. 5).

If a simple weighting is adopted, $w_i = \dfrac{1}{4}, \quad i = 1, 2, 3, 4$. Then $n_e^{light} \sim n_e^{node} \sim n_e^{heavy}$. Compared to the mass-weighted interpolation algorithm, the gradients near light materials are substantially reduced. Figure 6 shows that an abnormally high magnetic field peak appears near the interface when the mass-weighted average is adopted (the blue part indicates the strong magnetic field at the light-heavy interface), which eventually causes the simulation to diverge. In contrast, Fig. 7 uses a simple weighted average; its magnetic field distribution conforms to physical expectations and provides practical numerical simulation results.

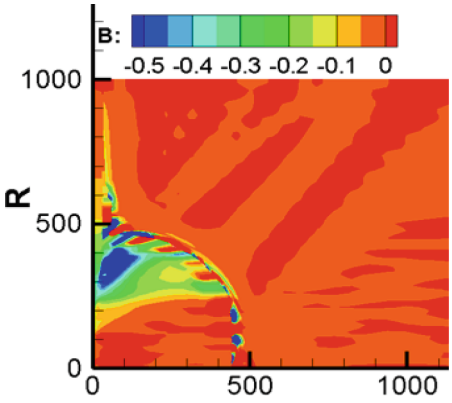


Fig. 6. Mass-weighted averaging causing non-physical magnetic fields near interfaces.

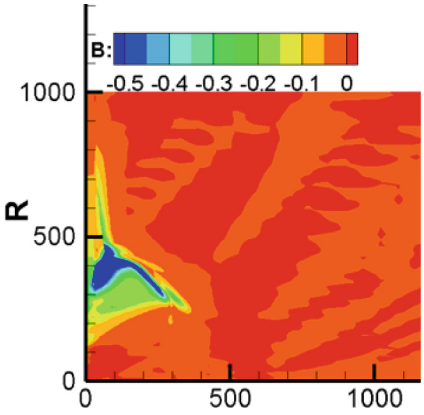


Fig. 7. Physically reasonable magnetic field distribution obtained by simple interpolation.

4.2 Least-Squares Scheme

In the coupled simulation of magnetic fields and radiation hydrodynamic equations, although the loop integral discrete scheme can yield roughly reasonable simulation results, numerical oscillations will occur in long-term Lagrangian simulations. To suppress the oscillatory behavior of the scheme, we design a novel discrete approach. We reformulate the Biermann term as follows:

$$\frac{c}{e}\nabla \times (k_B T_e \nabla \ln n_e) = \frac{ck_B}{e}\nabla T_e \times \nabla \ln n_e. \tag{11}$$

Starting from Eq. (11), we directly reconstruct gradients of electron number density and temperature on the grid. Conventional gradient reconstruction mostly adopts cell-centered and edge-centered quantities within the local grid cell. It features a simple stencil structure and low computational cost, yet fails to effectively utilize the characteristics of diagonal flow fields. In cases of slight grid distortion, large gradient variations of flow fields or discontinuity regions, gradient fitting is prone to numerical oscillation and accuracy degradation.

In this new scheme, taking the target grid cell as the center, a total of 9 cells in the surrounding 3×3 nine-grid scheme are selected to construct the reconstruction stencil. Neighboring cells are involved in gradient fitting, which greatly increases the constraint redundancy. The overdetermined system is solved by the least squares method to improve the stability of gradient reconstruction. This large-stencil structure delivers better computational performance for distorted and skewed grids.

Assuming electron temperature and electron number density follow linear distributions over adjacent nine-grid cells,

$$f(x) = a_1 x + a_2 z + a_3,$$

we approximate the distribution function via least-squares minimization by solving the following optimization problem,

$$minimize\{a_i, i = 1, 2, 3 \Big| \sum_{j=1,\cdots,9} \|f_j - (a_1 x_j + a_2 z_j + a_3)\|^2 \}. \tag{12}$$

where $(x_j, z_j),\ j = 1, \cdots, 9$ denotes coordinates of adjacent nine-grid cell centers, f_j and corresponds to either T_{ej}or $\ln n_{ej}$. This yields gradient distributions for electron number density and electron temperature. It should be noted that the electron number density here constructs a linear distribution of its logarithmic function. It is called Scheme 2 or the new scheme.

5 Numerical Test

The two discrete schemes proposed in the previous section were tested using an exact solution model to evaluate their performance across different grid types. The computational accuracy of the schemes was demonstrated for both orthogonal grids and general distorted grids. The algorithm was further applied to coupled simulations of realistic magnetic fields and radiation hydrodynamics equations to examine its overall performance.

Model 1. Accuracy Solution Model
Supposed that the control equation is

$$\frac{\partial B}{\partial t} = \frac{ck_B}{en_e} \nabla T_e \times \nabla n_e.$$

The initial distribution is $Te = 2 + cos(\pi y)/\pi$, $lnNe = 2 - cos(\pi x)/\pi$. Then the analysis solution is $B = -sin(\pi x)sin(\pi y)$.

The two discrete schemes proposed in the previous section were first tested using an exact solution model to evaluate their performance across different grid types. The computational accuracy of the schemes was demonstrated for both orthogonal grids and general distorted grids. The algorithm was further applied to coupled simulations of realistic magnetic fields and radiation hydrodynamics equations to examine its overall performance.

Based on the different grid types in the region $\Omega = [0, 1] \times [0, 1]$ the two schemes are tested, Fig. 8 shows the contour distribution of magnetic field intensity for the scheme1 on orthogonal grids and general distorted grids. It can be seen that the algorithm preserves the physical solution's contour distribution well on orthogonal grids. However, on general distorted grids, the numerical results exhibit significant oscillations, failing to maintain the physical solution's contour distribution. Accuracy tests across various grid resolutions reveal that the original algorithm achieves 1.5-order convergence accuracy on orthogonal grids but fails to achieve a meaningful convergence order on general distorted grids (see

Table 1. Accuracy Order of Scheme 1

Mesh	L2 Error (orthogonal grids)	L2 Order	L2 Error (general distorted)	L2 Order
20 × 20	6.537E-3	–	1.743E-2	–
40 × 40	2.167E-3	1.59	1.851E-2	–
80 × 80	7.351E-3	1.56	1.730E-2	–

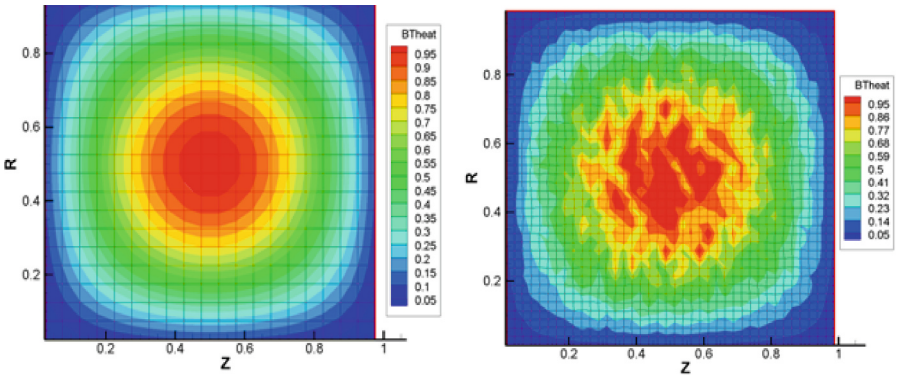


Fig. 8. Magnetic field intensity distribution on orthogonal grid (left) and randomized grid (right).

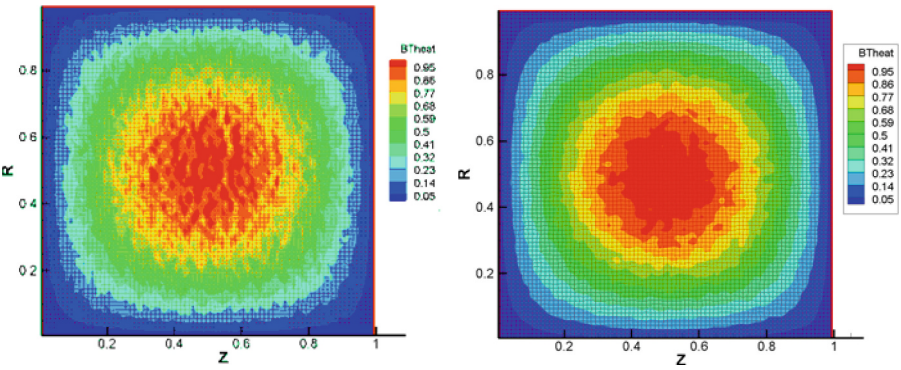


Fig. 9. Magnetic field intensity distribution on randomized grid by scheme 1 (left) and scheme 2 (right).

Table 2. Accuracy Order of Scheme 2

Mesh	L2 Error (orthogonal grids)	L2 Order	L2 Error (general distorted)	L2 Order
20 × 20	4.256E-2	–	4.375E-2	–
40 × 40	1.983E-2	1.1	2.099E-2	1.05
80 × 80	9.502E-3	1.06	1.104E-2	0.93

Table 1). This indicates that in Lagrangian computations, grid distortion easily triggers numerical oscillations in the Biermann discrete scheme.

Figure 9(left) and (right) present numerical solutions of the original and new algorithms on a 80 × 80 randomized grid respectively. The original algorithm exhibits significant oscillations, while the new algorithm effectively suppresses numerical oscillations and maintains contour distribution of magnetic field intensity. Precision tests demonstrate that the new algorithm achieves first-order convergence accuracy on both orthogonal and general randomized grids (see Table 2). Although slightly less accurate compared to orthogonal grids, this algorithm demonstrates superior precision and adaptability on Lagrangian grids.

Model 2. Laser Ablation Au Target Model
Computational domain is $[0, 30\mu m] \times [0, 100\mu m]$, grid size is 200 × 10, laser energy is $231.73J$, focal spot radius is 50 μm. The radiation transport coupled with self-generated magnetic field is used to simulate the model.

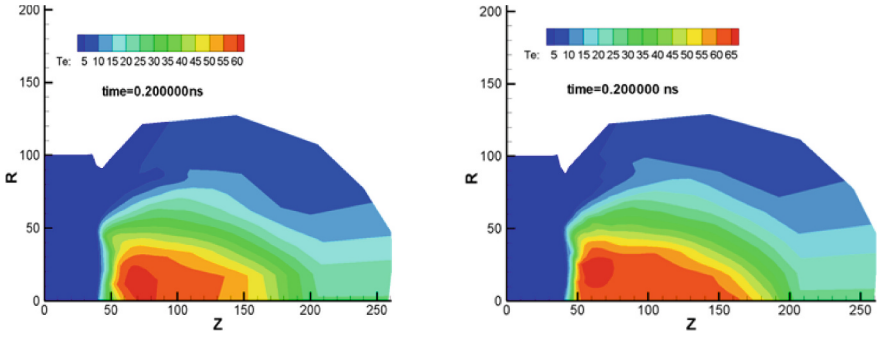


Fig. 10. Electron temperature contour by scheme 1 (left) and scheme 2 (right).

Figures 10 and 11 present the electron temperature and magnetic field intensity distributions obtained using the original algorithm and the new algorithm, respectively. The figures reveal that compared to the original algorithm, the overall distributions of electron temperature and magnetic field intensity obtained with the new algorithm show minor differences. However, the peak magnetic field values are slightly reduced, while the peak electron temperature values exhibit a modest increase.

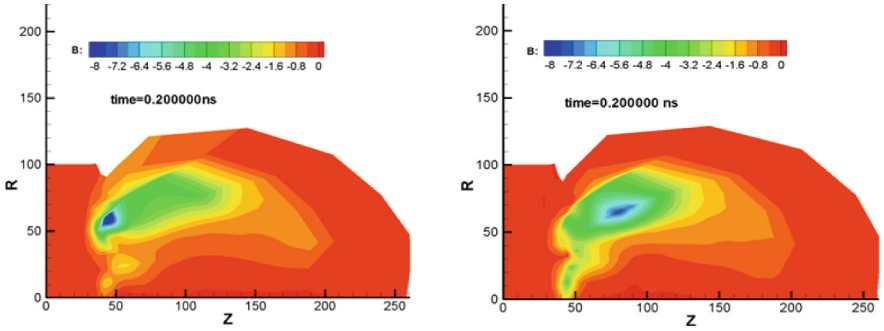


Fig. 11. Magnetic field intensity contour by scheme 1 (left) and scheme 2 (right).

Model 3. Cylindrical Hohlraum Model

The size of the cylindrical hohlraum is $1040\mu m \times 100\mu m$, with the cavity wall made of Au (initial density $19.24g/cm^3$) and a thickness of $20\mu m$. The hohlraum is filled with low-density Au gas (initial density $0.0008g/cm^3$) at an initial temperature of $300K$. The laser injection port has a diameter of $800\mu m$ and an incident angle of 45, with an energy of $2kJ$. The laser adopts a trapezoidal pulse, with a rising edge of $300ps$, a waveform duration of $1ns$, and a wavelength of $0.35\mu m$. The radiation transport coupled with self-generated magnetic field is used to simulate the model.

Figures 12, 13, 14 and 15 compare the electron temperature and magnetic field intensity distributions obtained with the original algorithm and the new algorithm respectively. The magnetic field intensity distribution demonstrates significantly reduced oscillations and lower peak values under the new algorithm. The electron temperature distribution obtained with the new algorithm shows minor differences from the original algorithm. These results indicate that the new algorithm effectively suppresses nonphysical oscillations in the magnetic

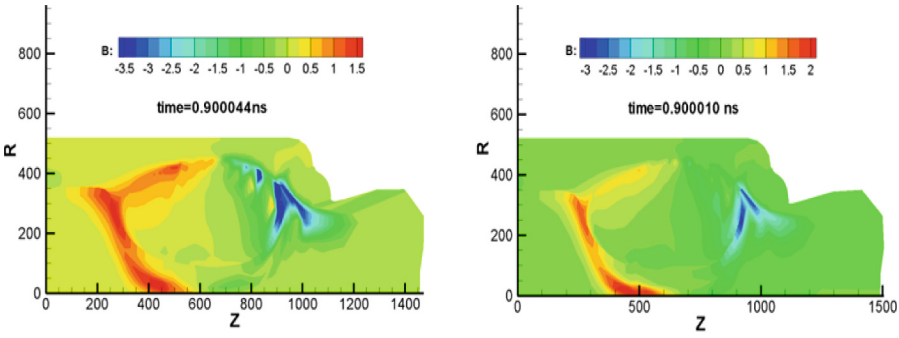


Fig. 12. Magnetic field intensity contour by scheme 1 (left) and scheme 2 (right).

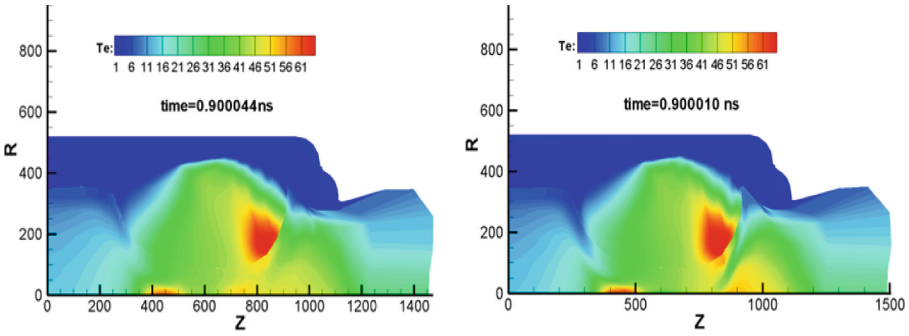


Fig. 13. Electron temperature contour by scheme 1 (left) and scheme 2 (right).

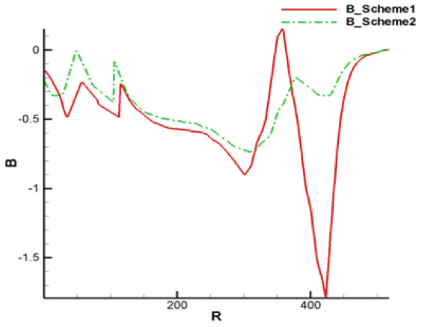


Fig. 14. Magnetic field intensity compare along z = 400.

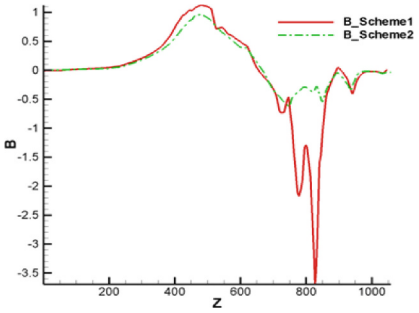


Fig. 15. Magnetic field intensity compare along r = 200.

field. Simultaneously, the new algorithm yields reduced magnetic field intensity and slightly elevated electron temperatures.

6 Conclusion

This paper presents a numerical simulation study on the Biermann-Battery term of self-generated magnetic fields. Through analyzing Biermann-Battery term in practical application simulations, two types of finite-volume discrete scheme and the corresponding nodal quantity interpolation method are proposed. The computational accuracy and oscillation suppression performance of both schemes are compared, with algorithm effectiveness verified in practical simulations.

Acknowledgments. This work has been partially supported by the National Science Foundation of China (No. 12101067.)

Disclosure of Interests. The authors have no competing interests to declare that are relevant to the content of this article.

References

1. Farmer, W.A., et al.: Simulation of self-generated magnetic fields in an inertial fusion Hohlraum environment. Phys. Plasmas **24**, 052703 (2017)
2. Gao, L., Nilson, P.M., Igumenshchev, I.V., et al.: Precision mapping of laser-driven magnetic fields and their evolution in high-energy-density. Phys. Rev. Lett. **114**, 215003 (2015)
3. Raphael, Plasma Physics, NNT:2016SACLX004 (2016)
4. Li, C.K.: Phys. Rev. Lett. **97**, 135003 (2006)
5. Wolff, M.: Mathematical and numerical analysis of the resistive magnetohydrodynamics system with self-generated magnetic field terms, PhD Thesis, Université de Strasbourg (2011)
6. Jia, J.-Y., Held, E.D.: Closure and transport theory for high-collisionality electron-ion plasmas. Phys. Plasmas **20**, 042114 (2013)
7. Fatenejad, M., et al.: Modeling HEDLA magnetic field generation experiments on laser facilities. High Energy Density Phys. **9**, 172–177 (2013)
8. Xu, H., O'Shea, B., et al.: The Biermann battery in cosmological MHD simulations of population III star formation. Astrophys. J. **688**, 2 (2008)
9. Graziani, C., et al.: The Biermann catastrophe in numerical magnetohydrodynamics. Astrophys. J. **802**, 1 (2015)
10. Armstrong, A.P., et al., Numerical demonstration of Biermann-generated magnetic fields in a laser-driven cylindrical implosion platform. Phys. Plasmas **32**, 072705 (2025)
11. Fryxell, B.: FLASH: an adaptive mesh hydrodynamics code for modeling astrophysical thermonuclear flashes. Astrophys. J. Suppl. Ser. **131**, 273–334 (2000)